Large-Eddy Simulation: How Large is Large Enough?

STEPHAN R. DE ROODE AND PETER G. DUYNKERKE*

Institute for Marine and Atmospheric Research Utrecht, University of Utrecht, Utrecht, Netherlands

HARM J. J. JONKER

Thermofluids Section, Department of Applied Physics, Delft University of Technology, Delft, Netherlands

(Manuscript received 3 December 2002, in final form 2 September 2003)

ABSTRACT

The length scale evolution of various quantities in a clear convective boundary layer (CBL), a stratocumulus-topped boundary layer, and three radiatively cooled (''smoke cloud'') convective boundary layers are studied by means of large-eddy simulations on a large horizontal domain (25.6×25.6 km^2). In the CBL the virtual potential temperature and the vertical velocity fields are dominated by horizontal scales on the order of the boundary layer depth. In contrast, the potential temperature and the specific humidity fields become gradually dominated by mesoscale fluctuations. However, at the mesoscales their effects on the virtual potential temperature fluctuations nearly compensate. It is found that mesoscale fluctuations are negligibly small only for conserved variables that have an entrainment to surface flux ratio close to -0.25, which is about the flux ratio for the buoyancy. In the CBL the moisture and potential temperature flux ratios can have values that significantly deviate from this number.

The geometry of the buoyancy flux was manipulated by cooling the clear convective boundary layer from the top, in addition to a positive buoyancy flux at the surface. For these radiatively cooled cases it is found that both the vertical velocity as well as the virtual potential temperature spectra tend to broaden. The role of the buoyancy flux in their respective prognostic variance equations is discussed. It is argued that in the upper part of the clear CBL, where the mean vertical stratification is stable, vertical velocity variance and virtual potential temperature variance cannot be produced simultaneously. For the stratocumulus case, in which latent heat release effects in the cloud layer play an important role in its dynamics, the field of any quantity, except for the vertical velocity, becomes dominated by mesoscale fluctuations.

In general, the location of the spectral peak of any quantity becoming constrained by the domain size should be avoided. The answer to the question of how large the LES horizontal domain size should be in order to include mesoscale fluctuations will, on the one hand, depend on the type of convection to be simulated and the kind of physical question one aims to address, and, on the other hand, the time duration of the simulation. Only if one aims to study the dynamics of a dry CBL that excludes moisture, a rather small domain size suffices. In case one aims to examine either the spatial evolution of the fields of any arbitrary conserved scalar in the CBL, or any quantity in stratocumulus clouds except for the vertical velocity, a larger domain size that allows the development of mesoscale fluctuations will be necessary.

1. Introduction

From an analysis of the horizontal wind velocities Van der Hoven (1957) found a local minimum in the spectral energy at wavelengths in the mesoscale range. As such the concept of the ''spectral gap'' was introduced, which is supposed to separate small-scale turbulent fluctuations from the larger mesoscale and synoptic perturbations. Accordingly, turbulent processes in convective atmospheric boundary layers, devoid of large-scale forcings, are thought to operate in a large, yet confined, scale range delineated by the dissipation scale ($\sim$1 mm) on the one hand and the depth of the planetary boundary layer ($\sim$1 km) on the other hand. Eddies with a scale larger than the depth of the planetary boundary layer are supposed not to occur, and hence all turbulence variables (including temperature and moisture) are assumed not to exhibit fluctuations in the mesoscale range (scales $>$ 1 km).

However, in contrast to this view, various field experiments performed in both clear and cloudy boundary layers have shown that generally a significant amount of variance is present at the mesoscales for quantities such as moisture, temperature, or the horizontal wind components (e.g., Nicholls and LeMone 1980; Roth-

* Deceased.

Corresponding author address: Stephan R. de Roode, Institute for Marine and Atmospheric Research Utrecht, University of Utrecht, Princetonplein 5, 3584 CC Utrecht, Netherlands.
E-mail: roode@phys.uu.nl

ermel and Agee 1980; Nucciarone and Young 1991; Davis et al. 1996; Jonker et al. 1997; Young 1987; Durand et al. 2000). Typically only the vertical velocity spectrum is found to exhibit a classical shape: a spectral peak at a length scale close to the boundary layer depth and a gradually decreasing spectral variance following a $-5/3$ slope to larger wavenumbers in the inertial subrange. Mesoscale perturbations are usually minimal for vertical velocity due to the shallowness of the atmosphere.

In many cases the presence of fluctuations on the mesoscales is clearly visible from satellite images (e.g., Agee 1984; Atkinson and Zhang 1996; Shao and Randall 1996). An example of an extended stratocumulus cloud deck above the Pacific Ocean off the coast of California is shown in Fig. 1. The low clouds are supplied with a significant input of moisture from the ocean's surface that is effectively trapped by a very stable inversion at about 500 $\sim$ 1000 m. Despite the shallow depth of the stratocumulus-topped boundary layer (STBL) the cloud cell sizes tend to grow, while the clouds are advected southward, to values of approximately 10 $\sim$ 20 km. These kinds of large-scale cloud patterns cover a considerable part of the earth's atmosphere, exhibiting a very distinct organization (Agee 1984; Atkinson and Zhang 1996). This phenomenon, called mesoscale shallow convection, includes cloud streets as well as cell patterns, the latter being referred to as mesoscale cellular convection (MCC). MCC comprises cells with a typical depth of a few kilometers, but with typical diameters ranging from 10 to 100 km. Nevertheless they are considered as manifestations of boundary layer processes, and hence as boundary layer phenomena.

Apart from being an intriguing physical problem, the presence of mesoscale fluctuations has important implications on the analysis of field observations (Duynkerke and de Roode 2001; Mahrt et al. 2001), large-scale modeling studies and large-eddy simulation (LES). The presence of mesoscale fluctuations may lead to considerable complications in the analysis of turbulence from field observations since it requires a much longer measurement length to obtain results with a sufficient accuracy (Lenschow and Stankov 1986; Lenschow et al. 1994). Should one apply a filter to observational data in order to separate the mesoscale from the turbulent fluctuations (Nicholls 1989), then the magnitude of the variance becomes dependent on the choice of the filter length scale. A similar problem arises in numerical weather prediction models in which processes smaller than the grid size need to be parameterized, in particular if the grid distance does not fall within the spectral gap range. In that case the magnitude of the unresolved (co)variance, like the vertical flux of moisture or passive scalars (tracers), becomes dependent of the horizontal grid distance. Last, it means that the horizontal domain size of an LES model must be sufficiently large to be capable to represent mesoscale structures (Müller and Chlond 1996; Schröter and Raasch 2002). As indicated by the title of the present paper—which paraphrases the title of the paper by Lenschow et al. (1994)—one may wonder how large the horizontal domain should be. Because, as will be shown, if one waits long enough, domain size fluctuations will sooner or later start to play an important, if not dominating, role.

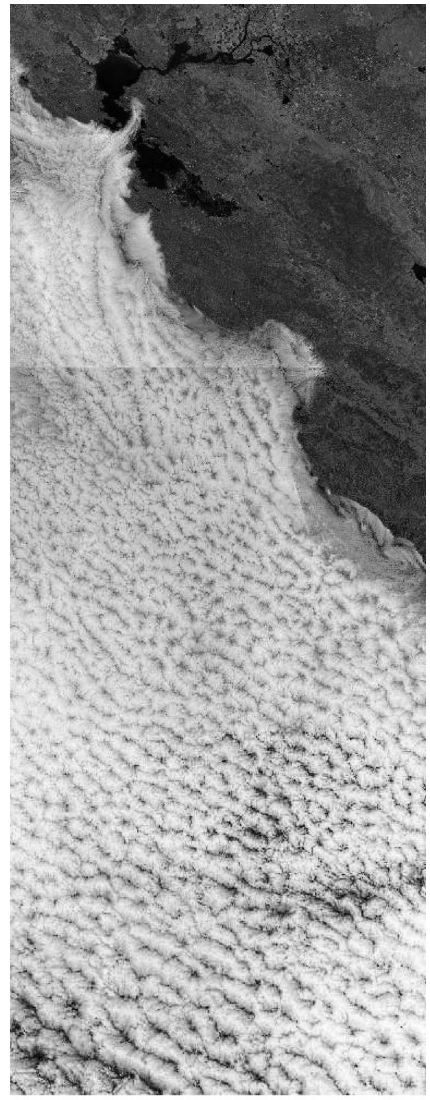

FIG. 1. Landsat satellite image (domain size about 200 $\times$ 600 km^2) showing stratocumulus off the coast of California 14 Jul 1987. The cloud tops are at 500 $\sim$ 1000 m whereas the convective cells have a horizontal dimension of about 10 km. The aspect ratio of the convective cells is thus much larger than 1.

Much research has been devoted to explain the development of fluctuations at the mesoscales. These investigations have been carried out by various research groups employing a variety of techniques, including observational, theoretical, experimental (Krishnamurti and Howard 1981), and numerical methods (Sykes et al. 1988). Comprehensive reviews of contributions to this topic can be found in VanDelden (1992) and Atkinson and Zhang (1996). Atkinson and Zhang discuss six different physical mechanisms that may be responsible for the generation of mesoscale fluctuations. They include the effects of anisotropy of eddy diffusivities, mesoscale entrainment instability, boundary conditions, upscale transfer of turbulent kinetic energy, gravity waves, and latent heat. However, the authors conclude that the roles and interplay of the processes in the evolution of mesoscale shallow convection remain unclear and remark that three-dimensional models, with domain sizes large enough to capture the mesoscale structures in their larger contexts and with spatial resolutions fine enough to capture the internal behavior of the rolls and cells, probably offer the best opportunity for elucidating the mechanisms.

Examples of such numerical studies are reported by Fiedler (1993), Fiedler and Khairoutdinov (1994), Müller and Chlond (1996), Shao and Randall (1996), Dörnbrack (1997), and Jonker et al. (1999a). Müller and Chlond (1996) simulated a cold air outbreak using LES. They concluded that diabatic processes such as latent heat release due to condensation, but in particular radiative cooling at the cloud top are essential ingredients for cell broadening. By contrast, Dörnbrack (1997) revealed that cell broadening also takes place in an LES of the dry convective boundary layer. His simulation was based on the so-called nonpenetrative dry boundary layers, that is, a convective boundary layer with a rigid lid on top. Dörnbrack concluded that additional heating or cooling in the bulk of the CBL leads to a broadening of convective cells due to an increase in the buoyancy flux, which in turn enhances the total kinetic energy of the flow. Note that the findings of Müller and Chlond are in line with this conclusion since both radiative cooling at the top of the boundary layer and latent heat release tend to increase the buoyancy flux.

Recently it has turned out that the situation in the dry penetrative convective boundary layer (mixed layer capped by an inversion) is even more puzzling (Jonker et al. 1999a). Passive scalar (inert tracer) fields appear to undergo significant cell broadening, while at the same time the dynamically active fields, including buoyancy, do not broaden. In other words, the variance spectra of the dynamical variables exhibit a peak at the scale of the boundary layer depth, but simultaneously spectra of tracer fields peak at much larger scales (mesoscales). The scale enlargement of the tracer fields (i.e., shift of the spectral peak to smaller wavenumbers) does not always occur, but was found to critically depend on the flux geometry of the tracer, with the ratio between the entrainment flux and the surface flux of the tracer as the crucial parameter. Furthermore, in agreement with the findings of Dörnbrack (1997), this study demonstrated that even without diabatic processes like radiation or latent heat release, mesoscale structures can develop due to boundary layer convection only.

In this paper we will focus on the evolution of length scales of both dynamical quantities as well as passive scalars for a variety of different types of convective boundary layers. As a means we have performed large-eddy simulations on a large horizontal domain (25.6 × 25.6 km^2), which appears to be large enough to capture mesoscale structures. We follow a rather phenomenological approach: rather than focusing on the cause, we try to identify the necessary ingredients for the generation of mesoscale growth and study which processes enhance it. To this end, we will present results of a clear convective boundary, a stratocumulus-topped boundary layer, and three radiatively cooled (''smoke cloud'') convective boundary layers (e.g., Bretherton et al. 1999). Length scales are determined from the (co)variance spectra. We will consider the production terms in the variance equations for the vertical velocity and the virtual potential temperature. Since the buoyancy flux is an essential element of both production terms, we have applied a cooling rate at the top of a clear convective boundary layer in order to systematically explore its role on the evolution of the length scales. Finally we discuss the consequence of strong mesoscale fluctuations in relation to the horizontal size of the computational domain.

2. Setup of the simulations

a. Model formulation

The large-eddy simulations have been performed with the Institute for Marine and Atmospheric Research Utrecht/Royal Netherlands Meteorological Institute (IMAU/KNMI) model (Cuijpers 1994; Siebesma and Cuijpers 1995; VanZanten 2000). The filtered prognostic equations for the resolved part of an arbitrary conserved quantity χ and the velocity u_i read, respectively,

$$\frac{\partial \chi}{\partial t} = -\frac{\partial u_j \chi}{\partial x_j} - \frac{\partial \overline{u_j'' \chi''}}{\partial x_j} + S_\chi, \quad (1)$$

$$\frac{\partial u_i}{\partial t} = \frac{g}{\theta_0}(\theta_v - \theta_0)\delta_{i3} - \frac{\partial u_i u_j}{\partial x_j} - \frac{\partial \pi}{\partial x_i} - \frac{\partial \tau_{ij}}{\partial x_j}, \quad (2)$$

where $\overline{u_j'' \chi''}$ and τ_{ij} are the subgrid flux terms and π is the modified pressure (Deardorff 1973). In the LES model the subgrid fluxes are expressed as the product of an eddy viscosity or eddy diffusivity and the local gradient of the resolved variable. The eddy diffusivities of the passive scalars are identical.

Details of the simulations can be found in Table 1. The horizontal spacing was 100 m and the vertical grid spacings were Δz = 20 m for the clear convective boundary layers on 256 × 256 × 96 grid points and Δz = 15 m for the stratocumulus simulation on 256 × 256 × 80 grid points. The stratocumulus case is based on observations made during the First International Satellite Cloud Climatology Project (ISCCP) Regional Experiment (FIRE I; Albrecht et al. 1988; Hignett 1991). Radiosonde observations have been used to initialize

TABLE 1. Summary of the initialization values used for the large-eddy simulation of a convective boundary layer (CBL), stratocumulus, and three radiatively cooled dry convective boundary layers (smoke 1–3). The subscript BL indicates a constant value within the boundary layer, Δ the jump across the inversion, GEO the geostrophic wind velocity, d/dz_{FA} the vertical gradient above the inversion in the free atmosphere, and the subscript 0 the value of the flux at the surface. The variables ψ and ϕ represent the bottom-up and top-down scalar, respectively.

	CBL	Stratocumulus	Smoke 1–3	Units
p_{surf}	1040.0	1012.5	1000.0	hPa
Inversion base	810.0	577.5	850.0	m
Inversion top	830.0	592.5	870.0	m
U_{geo}	0.001	3.4	0.0	m s^{-1}
V_{geo}	0.0	-4.9	0.0	m s^{-1}
$d/dz\langle W\rangle$	0.0	-1×10^{-5}	0.0	s^{-1}
$\langle U\rangle_{BL}$	0.001	3.4	0.0	m s^{-1}
$\Delta\langle U\rangle$	0.0	0.0	0.0	m s^{-1}
$\langle V\rangle_{BL}$	0.0	-4.9	0.001	m s^{-1}
$\Delta\langle V\rangle$	0.0	0.0	-0.001	m s^{-1}
$\langle q_t\rangle_{BL}$	16.0	9.6	0.0	g kg^{-1}
$\Delta\langle q_t\rangle$	-14.0	-3.0	0.0	g kg^{-1}
$d/dz\langle q_t\rangle_{FA}$	0.0	-3.0	0.0	g kg^{-1} km^{-1}
$\langle\theta_l\rangle_{BL}$	305.0	287.5	288.0	g kg^{-1}
$\Delta\langle\theta_l\rangle$	5.0	12.0	7.0	K
$d/dz\langle\theta_l\rangle_{FA}$	12.26	7.5	0.0	K km^{-1}
$\langle\psi\rangle_{BL}$	1.0	1.0	1.0	
$\Delta\langle\psi\rangle$	0.0	0.0	0.0	
$d/dz\langle\psi\rangle_{FA}$	0.0	0.0	0.0	km^{-1}
$\langle\phi\rangle_{BL}$	1.0	1.0	1.0	
$\Delta\langle\phi\rangle$	0.1	0.1	0.1	
$d/dz\langle\phi\rangle_{FA}$	0.0	0.0	0.0	km^{-1}
$\langle w'q_l'\rangle_0$	1.366×10^{-1}	1.09×10^{-2}	0.0	(g kg^{-1}) (m s^{-1})
$\langle w'\theta_t'\rangle_0$	0.025	0.0013	0.05	m K s^{-1}
$\langle w'\theta_v'\rangle_0$	0.053	0.0032	0.05	m K s^{-1}
$\langle w'\psi'\rangle$	0.001	0.001	0.001	m s^{-1}
$\langle w'\phi'\rangle$	0.0	0.0	0.0	m s^{-1}
u_*	0.01	0.18	0.01	m s^{-1}

the vertical mean profiles of the potential temperature and the specific humidity (Duynkerke and Teixeira 2001). The stratocumulus case discussed in this paper is representative for a nocturnal cloud deck since we have not included solar radiative absorption in the LES model. The longwave radiative flux F is computed from the following expression,

$$F(x, y, z) = \Delta F_t e^{-a\mathrm{LWP}(x,y,z,z_t)}, \qquad (3)$$

where ΔF_t is the longwave radiative flux jump, $a = 130$ m^2 kg^{-1} a constant, z_t the top of the model domain, and LWP (x, y, z_1, z_2) the liquid water path in each vertical model column between z_1 and z_2,

$$\mathrm{LWP}(x, y, z_1, z_2) = \int_{z_1}^{z_2} \rho_0 q_l(x, y, z)\, dz, \qquad (4)$$

with $\rho_0 = 1.14$ kg m^{-3} the mean density and q_l the liquid water content. In addition, we have performed three simulations of clear convective boundary layers in which the turbulence is driven both from the surface as well as from the top by radiative cooling (smoke 1–3). These cases are inspired by the smoke cloud case discussed by Bretherton et al. (1999). The smoke cloud can be interpreted as a stratocumulus cloud deck in which latent heat release effects are excluded. Like stratocumulus, the smoke cloud is cooled just below the inversion (z_i) by a variation of the longwave radiation with height according to

$$z \le z_i: \quad F(z) = \Delta F_t e^{-aS(z,z_i)}, \qquad (5)$$

with $a = 0.02$ m^2 kg^{-1} and the "smoke path" S

$$S(z_1, z_2) = \int_{z_1}^{z_2} s\rho_0\, dz = \rho_0(z_2 - z_1), \qquad (6)$$

since in this study we use a constant value for the smoke concentration in the boundary layer, $s = 1$, and $s = 0$ above the inversion base. This approach leads to a cooling rate that is horizontally homogeneous. This is important in our case since we want to prevent that perturbations in the horizontal temperature field can be induced by horizontal fluctuations in the smoke field. By excluding this direct feedback we can better focus on effects due to changes in the shape of the heat flux profile induced by radiation, an effect which, as will turn out later, we consider much more relevant. The values applied for ΔF_t are summarized in Table 2.

b. Data analysis

1) FOURIER ANALYSIS AND LENGTH SCALE ANALYSIS

The spectral characteristics of the LES fields in the horizontal plane are analyzed from a Fourier transfor-

TABLE 2. Summary of key quantities for the simulated convective boundary layers at $t = 8$ h. Shown are the inversion height z_i, the convective velocity scale w_* according to Eq. (26), the vertically integrated virtual potential temperature flux, the vertically integrated variances for the vertical velocity and the virtual potential temperature. The vertical integration is applied over the whole vertical domain. The dominant length scales presented for the vertical velocity and the virtual potential temperature, $\Lambda_{\langle w'w'\rangle,\mathrm{mid}}$ and $\Lambda_{\langle\theta_v'\theta_v'\rangle,\mathrm{mid}}$, respectively, represent values for the middle of the boundary layer ($z/z_i = 0.5$). Also shown are the values used for ΔF.

Case	ΔF_t (W m^{-2})	z_i (m)	w_* (m s^{-1})	$\int \langle w'\theta_v'\rangle\,dz$ (m^2 K s^{-1})	$\int \langle w'w'\rangle\,dz$ (m^3 s^{-2})	$\int \langle \theta_v'\theta_v'\rangle\,dz$ (K^2 m)	$\Lambda_{\langle w'w'\rangle,\mathrm{mid}}/z_i$	$\Lambda_{\langle\theta_v'\theta_v'\rangle,\mathrm{mid}}/z_i$
CBL	0.0	1000	1.10	16.4	325.2	17.1	1.4	2.3
Smoke 1	20.0	980	1.15	18.5	354.8	20.3	1.5	2.9
Smoke 2	40.0	1020	1.21	21.7	410.8	30.8	1.8	5.5
Smoke 3	60.0	1040	1.27	25.6	454.4	43.2	1.9	7.9
Stratocumulus	70.0	570	0.65	3.4	47.7	48.8	2.5	21.2

mation, which provides a two-dimensional matrix of the (co)spectral density, $S_{\alpha\beta}(k_x, k_y)$. The wavenumbers k_x and k_y are then transformed to cylindrical coordinates (k, θ),

$$k_x = k\cos\theta, \qquad k_y = k\sin\theta, \tag{7}$$

where $k = (k_x^2 + k_y^2)^{1/2}$ and $\theta = \tan^{-1}(k_y/k_x)$, the angle between k_x and k_y $(0 \le \theta \le \pi)$. Finally, the (co)spectrum $S_{\alpha\beta}(k)$ is obtained by integrating out the dependency on θ,

$$S_{\alpha\beta}(k) = \int_{\theta=0}^{\theta=\pi} S_{\alpha\beta}(k\cos\theta, k\sin\theta)k\,d\theta. \tag{8}$$

Note that the total (co)variance satisfies

$$\langle\alpha'\beta'\rangle = \int_0^\infty S_{\alpha\beta}(k)\,dk. \tag{9}$$

A convenient tool to investigate scale characteristics is the ogive. For two arbitrary quantities α and β the ogive $O_{\alpha\beta}(k)$ is defined as the integral of the spectral density between the wavenumber k and the Nyquist frequency k_{Ny} (Oncley et al. 1996),

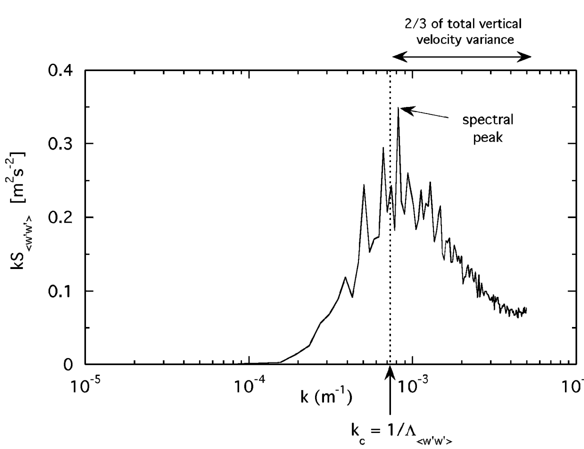

FIG. 2. Variance spectrum for the vertical velocity w in the middle of the boundary layer, $z/z_i = 0.5$. For this specific example the spectral peak is close to the critical wavenumber k_c, above which a 2/3 fraction of the total vertical velocity variance is located.

$$O_{\alpha\beta}(k) = \int_k^{k_{\mathrm{Ny}}} S_{\alpha\beta}(k)\,dk. \tag{10}$$

Thus the ogive gives the contribution to the covariance from all wavenumber components above wavenumber k. Note that $O_{\alpha\beta}(0) = \langle\alpha'\beta'\rangle$. To extract a length scale, we first compute the critical wavenumber k_c from

$$O_{\alpha\beta}(k_c) = \frac{2}{3}\langle\alpha'\beta'\rangle, \tag{11}$$

indicating that 2/3 of the variance resides at wavenumber higher than k_c. Next we define the length scale $\Lambda_{\alpha\beta}$ as

$$\Lambda_{\alpha\beta} = 1/k_c. \tag{12}$$

The interpretation is that 2/3 of the (co)variance resides at scales smaller than $\Lambda_{\alpha\beta}$ and 1/3 at scales larger than $\Lambda_{\alpha\beta}$. The definition of $\Lambda_{\alpha\beta}$ used is inspired by probability theory, where often a single parameter (modus, mean, or median) must represent an entire density. The procedure followed here is analogous to finding the ‘‘median’’ and has the advantage of being less sensitive to noise than, for instance, determining the spectral peak (‘‘modus’’). Figure 2 shows the length scale $\Lambda_{\langle w'w'\rangle}$ for the vertical velocity computed from its variance spectrum $S_{\langle w'w'\rangle}$ in the middle of the clear convective boundary layer. It is plotted in a log–linear fashion to account for the logarithmic wavenumber axis; in this way the area under the curve is equal to the total variance. The figure explains the choice of 2/3 in Eq. (11) since the spectral peak and k_c generally coincide for this value.

2) THE PRINCIPLE OF THE SUPERPOSITION OF VARIABLES

To diagnose the fields of an arbitrary passive scalar χ we will make use of the principle of superposition of variables (Wyngaard and Brost 1984). Let χ be given by a linear superposition of two variables ψ and ϕ and an arbitrary constant c,

$$\chi = a\psi + b\phi + c. \tag{13}$$

Note that the transport equation (1) of χ is linear in χ

(e.g., Jonker et al. 1999a). The boundary conditions for the variable ψ are chosen such that it has a nonzero surface flux, $\langle w'\psi'\rangle_0 \neq 0$, and a zero jump across the inversion causes a vanishing entrainment flux. Therefore, ψ is referred to as a bottom-up scalar. In contrast, the top-down scalar ϕ has a zero surface flux, $\langle w'\phi'\rangle_0 = 0$, but a nonzero entrainment flux $\langle w'\phi'\rangle_T$. This turbulent flux is generated due to a jump $\Delta\langle\phi\rangle$ initially applied across the inversion. After applying Reynolds decomposition on (13) and multiplication by w' we can express the vertical flux $\langle w'\chi'\rangle$ as a function of the bottom-up and top-down fluxes,

$$\langle w'\chi'\rangle = a\langle w'\psi'\rangle + b\langle w'\phi'\rangle. \qquad (14)$$

It is convenient to define ψ and ϕ such that they have unit surface flux and entrainment flux, respectively. By choosing appropriate values for a and b we can obtain any arbitrary flux ratio r, which is defined as the ratio of the entrainment to the surface flux of χ, indicated by the subscripts T and 0, respectively,

$$r = \frac{\langle w'\chi'\rangle_T}{\langle w'\chi'\rangle_0}. \qquad (15)$$

As long as the jump across the inversion of the bottom-up scalar is negligibly small, we have $r \approx b/a$. However, when the inversion jump $\Delta\psi$ becomes significant, ψ can no longer be considered as a "pure" bottom-up scalar since its flux will not vanish at the boundary layer top. In that case, we can reconstruct the field for a quantity with flux ratio $r = 0$, by letting the coefficient b satisfy

$$a\langle w'\psi'\rangle_T + b\langle w'\phi'\rangle_T = 0. \qquad (16)$$

A general formula for the variance $\langle\chi'^2\rangle$ can be expressed as

$$\langle\chi'^2\rangle = a^2\langle\psi'^2\rangle + b^2\langle\phi'^2\rangle + 2ab\langle\psi'\phi'\rangle. \qquad (17)$$

Similarly one finds for the variance spectrum of χ

$$S_{\chi\chi}(k) = a^2S_{\psi\psi}(k) + b^2S_{\phi\phi}(k) + 2abS_{\psi\phi}(k). \qquad (18)$$

This equation also implies that the length scale $\Lambda_{\chi\chi}$ can be derived from the spectra $S_{\psi\psi}(k)$, $S_{\phi\phi}(k)$ and the cospectrum $S_{\psi\phi}(k)$, for any choice of the variables a and b.

3. Results

a. The clear convective boundary layer

After 8 h of simulation the boundary layer depth (z_i) has risen to about 1000 m. Therefore, the aspect ratio (the horizontal domain size divided by the depth of the boundary layer) is about 25. Because of the large humidity flux from the surface and by the influence of moisture on the virtual potential temperature according to

$$\theta_v = \theta(1 + 0.61q), \qquad (19)$$

there is a rather strong deviation between the vertical flux profiles of the virtual potential temperature and the potential temperature. Since

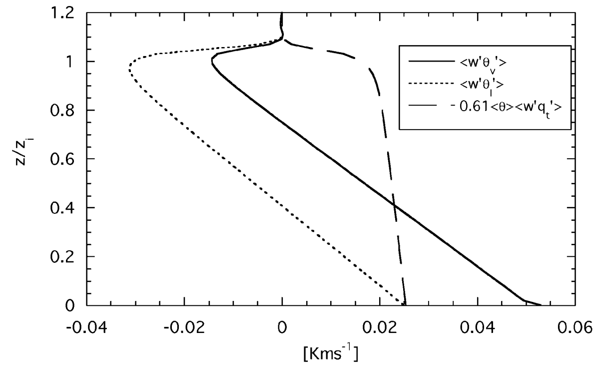

FIG. 3. Average vertical flux profiles for the virtual potential temperature θ_v, the potential temperature θ, and moisture q_t in the CBL during the last hour of the simulation ($7 < t \leq 8$ h). To show its contribution to the virtual potential temperature flux, the moisture flux has been multiplied by a factor $0.61\langle\theta\rangle$, according to Eq. (21).

$$\theta_v' \simeq \theta' + 0.61\langle\theta\rangle q', \qquad (20)$$

the virtual potential temperature flux reads, to a good approximation,

$$\langle w'\theta_v'\rangle = \langle w'\theta'\rangle + 0.61\langle\theta\rangle\langle w'q'\rangle. \qquad (21)$$

In Fig. 3 we show the vertical profile of the virtual potential temperature flux $\langle w'\theta_v'\rangle$, as well as the separate contributions to this flux from potential temperature, $\langle w'\theta'\rangle$, and from moisture, $0.61\langle\theta\rangle\langle w'q'\rangle$.

Figure 4 contains snapshots of the θ and θ_v fields in the middle of the CBL at $t = 8$ h. Quite remarkably, this figure reveals that the typical length scales for these quantities differ significantly. Both the vertical velocity and the virtual potential temperature fields are dominated by PBL depth structures, whereas the potential temperature and the specific humidity fields appear to be dominated by much larger length scales. On the basis of Fig. 4 two important conclusions can be drawn. First, mesoscale fluctuations can develop despite the fact that in the vertical velocity field and the buoyancy field similar structures appear to be nonexistent. Second, the length scales of the potential temperature and the specific humidity on the one hand, and the length scale of the virtual potential temperature on the other hand, differ significantly, despite the fact that fluctuations of these three quantities are intimately connected by (20). Interestingly, this finding implies that in the convective boundary layer mesoscale fluctuations may not only be present for passive scalars, as was already demonstrated by Jonker et al. (1999a), but also for thermodynamically *active* scalars like the temperature and moisture.

More quantitatively, in Fig. 5 the length scales of the various quantities, calculated according to Eqs. (10)–(12), are presented as a function of nondimensional height. Regarding vertical velocity, the maximum of $\Lambda_{\langle w'w'\rangle}$, about $\sim 1.4z_i$, is located just above the middle

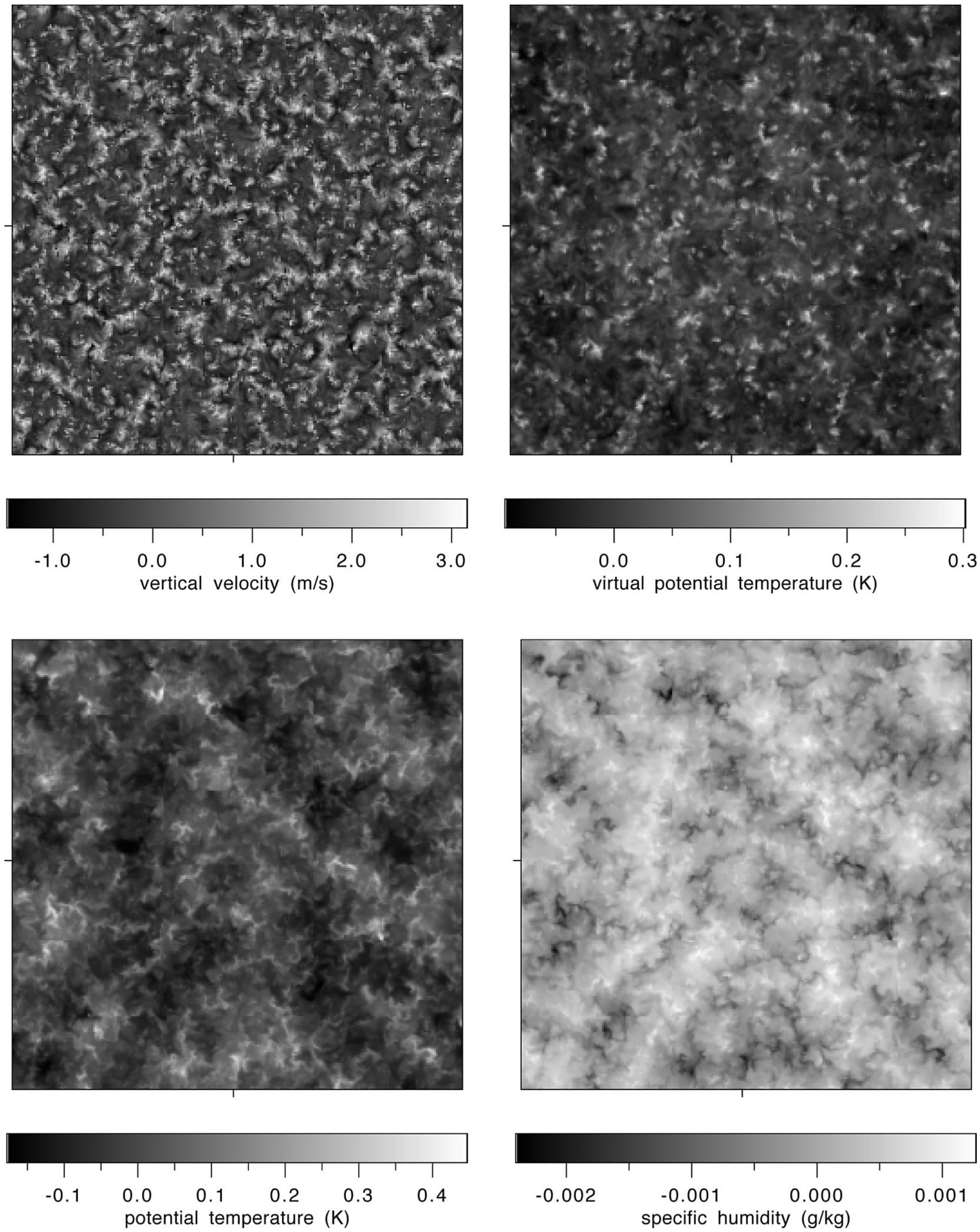

FIG. 4. Contour plots of (upper left) the vertical velocity, (upper right) the virtual potential temperature, (lower left) the potential temperature, and (lower right) the specific humidity in the middle of the CBL ($z/z_i = 0.5$) at $t = 8$ h.

of the boundary layer. It corroborates the notion that the vertical velocity variance is dominated by eddies that have scales on the order of the boundary layer depth. The variation of $\Lambda_{\langle w'w' \rangle}$ with height corresponds well with observations discussed by Kaimal et al. (1976) who showed that the spectral peak in the vertical velocity spectrum moves to larger wavelengths with increasing distance from the ground. Khanna and Brasseur (1998) determined the characteristic length scale from the integral length scale whereas Mason (1989) computed the value of the horizontal separation at which the two-point correlation for the vertical velocity has fallen to 0.36. The results of those LES studies compare well with the shape of the vertical profile of $\Lambda_{\langle w'w' \rangle}$. Furthermore, the LES results are in line with observations collected from aircraft in clear convective boundary layers. In general,

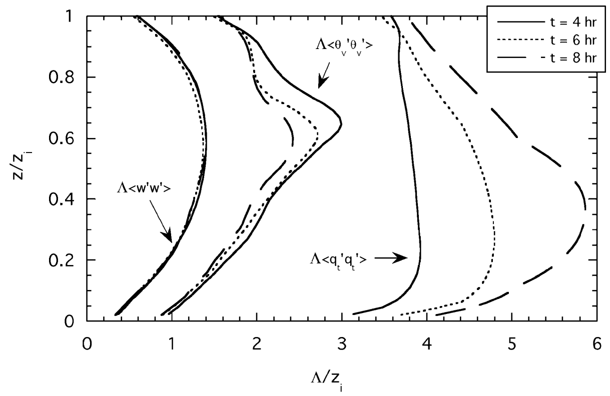

FIG. 5. Length scales normalized by the boundary layer depth (Λ/z_i) as a function of dimensionless height (z/z_i) for the CBL at t = 4, t = 6, and t = 8 h. Shown are the length scales for the vertical velocity $\Lambda_{\langle w'w'\rangle}$, the virtual potential temperature $\Lambda_{\langle \theta_v' \theta_v'\rangle}$, and the total specific humidity $\Lambda_{\langle q_t' q_t'\rangle}$. Line styles are according to the legend and are the same for the three variables. The arrows point to the length scales for the three different variables. The length scales for the vertical velocity are the smallest and are nearly identical, the virtual potential temperature length scales decrease slightly with time, whereas the length scales for the total specific humidity are much larger and increase significantly with time.

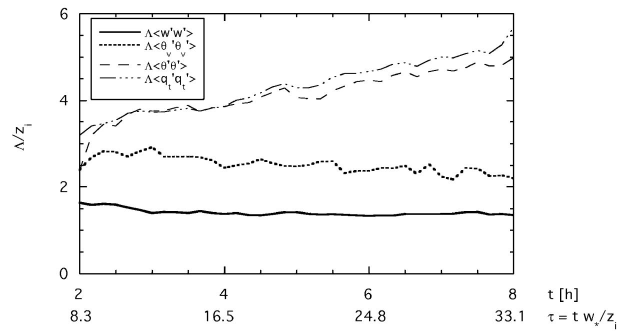

FIG. 6. Evolution of the length scale normalized by the boundary layer depth (Λ/z_i) in the middle of the CBL ($z/z_i = 0.5$) for the vertical velocity $\Lambda_{\langle w'w'\rangle}$, the virtual potential temperature $\Lambda_{\langle \theta_v' \theta_v'\rangle}$, the potential temperature $\Lambda_{\langle \theta' \theta'\rangle}$, and the total specific humidity $\Lambda_{\langle q_t' q_t'\rangle}$. The lower x-axis scale indicates the normalized, nondimensional time, $\tau = tw_*/z_i$. Line styles are according to the legend.

the vertical velocity spectrum is found to be dominated by eddies on order of the boundary layer depth (Nicholls 1978; Nicholls and LeMone 1980; Young 1987).

The length scale of θ_v is bit larger than that of w, but does not increase in time. By contrast, the length scales of moisture and potential temperature (not shown) are much larger, and increase significantly with time. Figure 6 conveys a similar message: the mid-PBL length scales of w and θ_v are stationary and scale well with z_i, whereas the length scales of q and θ continue to grow. This will proceed until the domain size exerts its influence, prohibiting further growth.

The disparity in the length scale behavior of different variables in the CBL has already been discussed by Jonker et al. (1999a). They stressed the importance of the corresponding flux profile and studied the length scale behavior as a function of the flux ratio—the ratio of the entrainment flux to the surface flux. In the middle of the CBL they found a distinct minimum length scale for a flux ratio near $r \approx -0.5$. We have conducted a similar analysis, the results of which are displayed in Fig. 7. Employing the superposition method, described in section 2, we calculated the length scale of the conserved variable χ for various flux ratios [see (15)] at t = 8 h. To show the entire range of flux ratios, we have made use of the ''angle'' φ:

$$\varphi = \arctan\left(\frac{1}{r}\right). \tag{22}$$

For flux ratios $|r| > 1$ the dominant length scale $\Lambda > 4z_i$. Recall that the figure is computed from the instantaneous fields at t = 8 h, meaning that after a longer simulation time even larger length scales will be found. Furthermore, note that there is no symmetry around r = 0. A range of minimum length scales between $z_i < \Lambda < 2z_i$ can be found at a flux ratio $r \approx -0.25$. This is the flux ratio of θ_v (see Fig. 3) and falls within the range of values typically found for the buoyancy flux (e.g., Stull 1988). In Fig. 7 we have also indicated the position (in terms of flux ratio) of the variables q and θ.

Examples of (co)spectra of the bottom-up and top-down scalars, the virtual potential temperature and the vertical velocity for the CBL are shown in Fig. 8. The presence of mesoscale fluctuations for the bottom-up and top-down scalars is well illustrated from the respective spectral density maxima after 8 h of simulation, which are located at about $k \approx 2 \times 10^{-4}$ m^{-1} (~5 km) for both quantities. Note, however, that the turbulent fluxes of these quantities are dominated by smaller scales, as revealed by the cospectra shown in Fig. 8b.

With the superposition principle it can be illustrated why the bottom-up and top-down scalars exhibit mesoscale fluctuations in contrast to the virtual potential temperature. With the appropriate values of a and b, Eq. (18) enables the reconstruction of the virtual potential temperature spectrum from the bottom-up and top-down spectra. Although the variance spectra for both the bottom-up and top-down scalars have a positive contribution at large scales, this is counteracted by the covariance term (since $b = -0.25a$). It means that for the buoyancy the mesoscale fluctuations generated separately by the surface and entrainment fluxes are anticorrelated to such an extent that they cancel (see Fig. 9). The strong anticorrelation has interesting consequences, on which we will come back below.

Rather than in terms of bottom-up and top-down processes, a more physical decomposition of θ_v fluctuations is given by (20) where they are expressed in terms of potential temperature and moisture fluctuations. Clearly, both q and θ exhibit a significant amount of variance at the mesoscales, as illustrated by their respective length scales depicted in Fig. 6a or by their spectra in Fig. 8. However, when they are linearly combined according to (20), the mesoscale contributions apparently

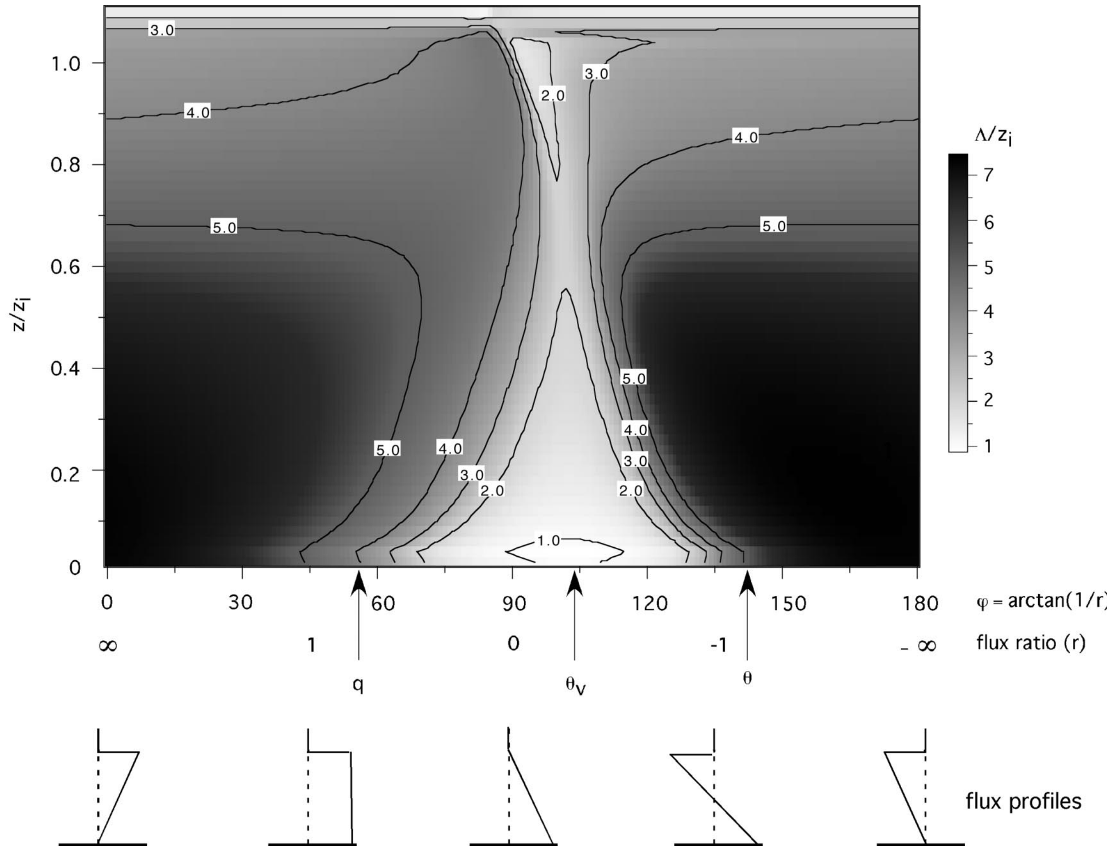

FIG. 7. Length scales normalized by the boundary layer depth (Λ/z_i) in the CBL at $t = 8$ h. The length scales are shown as a function of the dimensionless height (z/z_i) and the flux ratio angle φ according to Eq. (22). The lower x-axis label indicates a few corresponding flux ratios r, and the corresponding vertical flux profiles are displayed below. In addition, the flux ratios for the virtual potential temperature θ_v, the potential temperature θ, and the specific humidity q are indicated by the vertically pointing arrows.

vanish. From (20) an expression for the variance spectrum of θ_v can be derived similar to (18):

$$S_{\theta_v\theta_v}(k) = S_{\theta\theta}(k) + (0.61\langle\theta\rangle)^2 S_{qq}(k) + 2 \times 0.61\langle\theta\rangle S_{\theta q}(k). \tag{23}$$

The lack of mesoscale variance in θ_v implies directly that q and θ fluctuations must be anticorrelated to a high degree in that scale range. Indeed, if one equates the left-hand side of (23) to zero, the Fourier coefficients must satisfy $\hat{\theta}(k) = -0.61\langle\theta\rangle\hat{q}(k)$. This, in turn, implies two things for the mesoscale range. First, the variance spectra of potential temperature and specific humidity are isomorph:

$$S_{\theta\theta}(k) = (0.61\langle\theta\rangle)^2 S_{qq}(k), \tag{24}$$

and second, the mesoscale fluctuations of q and θ must be completely anticorrelated: the spectral correlation coefficient $\rho_{\theta q}(k) = -1$ for $k \ll 1/z_i$, where

$$\rho_{\theta q}(k) = \frac{S_{\theta q}(k)}{\sqrt{S_{\theta\theta}(k)}\sqrt{S_{qq}(k)}}. \tag{25}$$

That this is indeed the case can be observed from Fig. 9, which shows that at mesoscales $\rho_{\theta q}$ has values close to -1. In this context it is interesting to note that there is a direct analogy with the ocean mixed layer. Observations show that the temperature and salinity gradients on horizontal scales of 20 m to 10 km tend to compensate in their effect on the density (Rudnick and Ferrari 1999).

It must be emphasized that (24) and the strong anticorrelation are a consequence of the fact that *both* θ and q contain significant mesoscale fluctuations. This depends on the flux ratios r_θ and r_q. In Fig. 7 we have indicated the position of r_θ and r_q based on the present case. In the appendix we derive equations that express the flux ratios in terms of surface fluxes and inversion jumps of θ and q. Different boundary and jump conditions will therefore yield different flux ratios. By using Fig. 7 in combination with Eqs. (A3) and (A4), one can predict whether or not the new conditions will give rise to significant mesoscale fluctuations in q and/or θ.

b. *Stratocumulus*

The growth of the cloud scales in the simulation of the stratocumulus layer is illustrated from the liquid

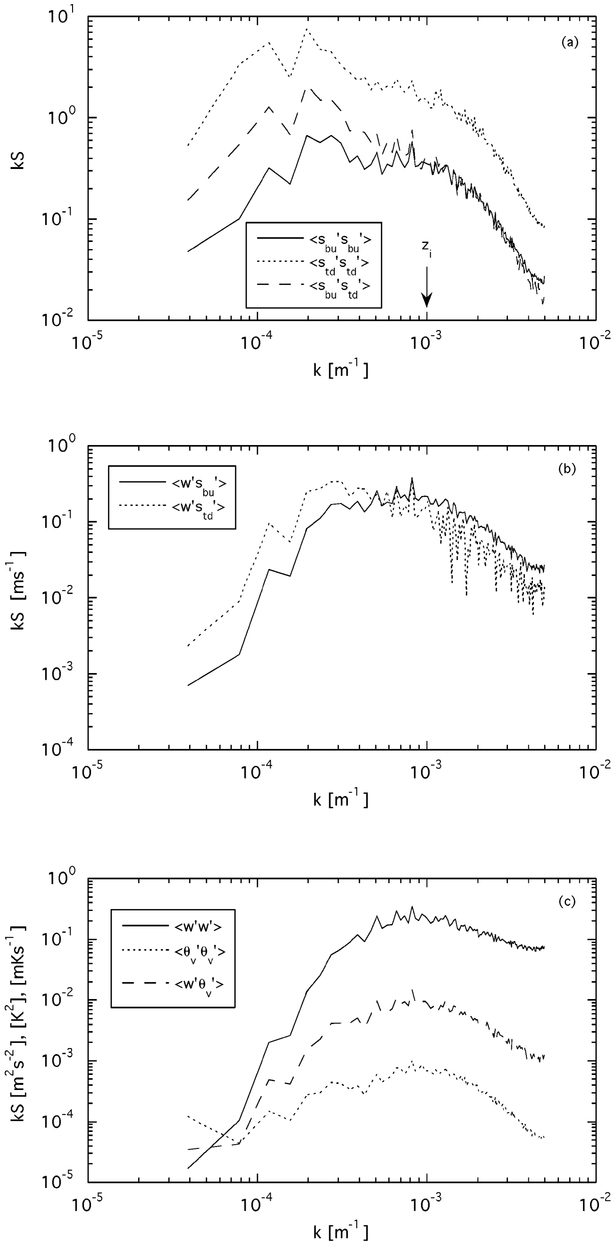

FIG. 8. (Co)variance spectra S multiplied by the wavenumber k in the middle of the CBL ($z/z_i = 0.5$) at $t = 8$ h. (a) Spectra for the bottom-up (s_{bu}) and top-down (s_{td}) scalars and their cospectrum. (b) Cospectrum of the bottom-up and top-down fluxes. (c) Spectra for the vertical velocity and virtual potential temperature, and their cospectrum. The wavenumber corresponding to the reciprocal of the boundary layer depth z_i is indicated by the vertically pointing arrow.

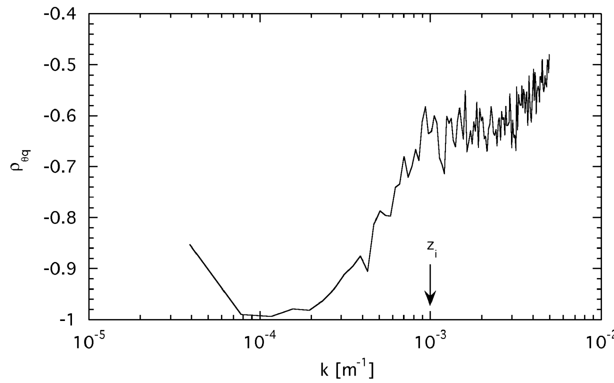

FIG. 9. Spectral correlation coefficient between the specific humidity and the potential temperature ρ_{θ_q}. The wavenumber corresponding to the reciprocal of the boundary layer depth z_i is indicated by the vertically pointing arrow.

water path images shown in Fig. 10. During the first 4 h of the simulation the cloud structures are organized in straight elongated coherent patterns that are approximately oriented along the mean wind vector. After 6 h the stratocumulus cloud is more cellular in its appearance, the typical cloud cell sizes are on order $5 \sim 10$ km.

Figure 11 shows that in the middle of the stratocumulus-topped boundary layer the length scale for the vertical velocity field exceeds twice the boundary layer depth and is, therefore, considerably larger than in the clear convective boundary layer. But the most important difference concerns the buoyancy fluctuations. In the CBL most of the buoyancy variance was contained by eddies of the order of the boundary layer depth, but for the stratocumulus case mesoscale fluctuations are clearly dominant (Fig. 11b).

An example of the time evolution of the variance in the middle of the boundary layer for several variables is shown in Fig. 12. The vertical velocity variance shows some relatively small fluctuations with time but there is no significant trend, indicating that the dynamical structure of the boundary layer is in an approximate steady state. The virtual potential temperature variance increases with time, as is the case for the variance of the total specific humidity and the bottom-up scalar. In contrast, the change in the variance of the top-down scalar is only minimal.

After 2 h of simulation the length scale of the vertical velocity field in the middle of the boundary layer becomes approximately constant with time, $\Lambda_{\langle w'w'\rangle} = 2.5z_i$, as can be seen in Fig. 13a. The length scales for all the other quantities shown in the same figure increase with time. After 8 h the top-down scalar has a length scale $\Lambda_{\langle s'_{td}s'_{td}\rangle} \approx 13z_i$, while for the virtual potential temperature $\Lambda_{\langle \theta'_v,\theta'_v\rangle} \approx 22z_i$.

An important consequence of the strong mesoscale fluctuations concerns their impact on the vertical convective transport: the vertical fluxes of various quantities have a significant contribution from these scales as well. For example, Fig. 13b shows that at the end of the simulation one-third of the total vertical flux of moisture is located at length scales larger than $\Lambda_{\langle w'q'_t\rangle} \approx 9z_i$. The figure also reveals that one-third of the total buoyancy flux results from fluctuations with length scales larger than $\Lambda_{\langle w'\theta'_v\rangle} \approx 15z_i$.

Finally, as a generalization of these results, Fig. 14 shows that mesoscale fluctuations in the variance spectra are present at all levels in the boundary layer and for all flux ratios.

c. The radiatively cooled (smoke cloud) convective boundary layers

Obviously, there are significant differences in the length scale behavior between the CBL and the stratocumulus case. Because the dynamical structure of stratocumulus is complicated due to the combination of latent heat release effects and longwave radiative cooling, it is difficult to assess the importance of a single mechanism on the length scale evolution. In contrast, the only difference between the smoke cloud and the CBL is the longwave radiative cooling at the top of the boundary layer such that any observed difference can be ascribed to radiative cooling.

The length scales $\Lambda_{\langle w'w'\rangle}$ and $\Lambda_{\langle\theta_v'\theta_v'\rangle}$ for the three smoke cloud cases are presented in Fig. 15. It is clear that longwave radiative cooling supports an increase in the length scales for w and θ_v. Both length scales are larger than found in the CBL but smaller than for stratocumulus.

These results are in qualitative agreement with the findings of Dörnbrack (1997) and Müller and Chlond (1996). Dörnbrack compared the length scale evolution for a convective boundary without entrainment, in addition to a boundary layer that was radiatively cooled. In the latter case, Dörnbrack found an increase in the growth rate of the thermal scales. Also, Müller and Chlond concluded that, in particular, longwave radiative cooling was a major process responsible for cell broadening, which was corroborated by Shao and Randall (1996) on the basis of two-dimensional model simulations.

Shao and Randall (1996), Müller and Chlond (1996), and Dörnbrack (1997) proposed various mechanisms explaining cell broadening. Dörnbrack, for example, concluded that broad temperature variances were caused by an increase in the vertical buoyancy flux profile and a subsequent increase in the turbulent kinetic energy due to cooling at the top of the boundary layer. Müller and Chlond (1996) and Shao and Randall (1996) suggested that an enhanced difference between the temperature in the updrafts and downdrafts, which may be caused by latent heat release effects as well, requires more heating from below in order to generate a positively buoyant updraft. This results in a longer average horizontal path of air parcels moving just above the warm sea surface thereby increasing the aspect ratio of the convection cells.

All these mechanisms proposed have in common that cell broadening can be explained by changes in the geometry of the buoyancy flux, in particular by an increase in the convective velocity scale w_* (see Table 2). In this study, it appears that cell broadening in the radiatively cooled convective boundary layers is caused by an enhancement of the buoyancy flux in the boundary layer, that is, an increase in the convective velocity scale w_*:

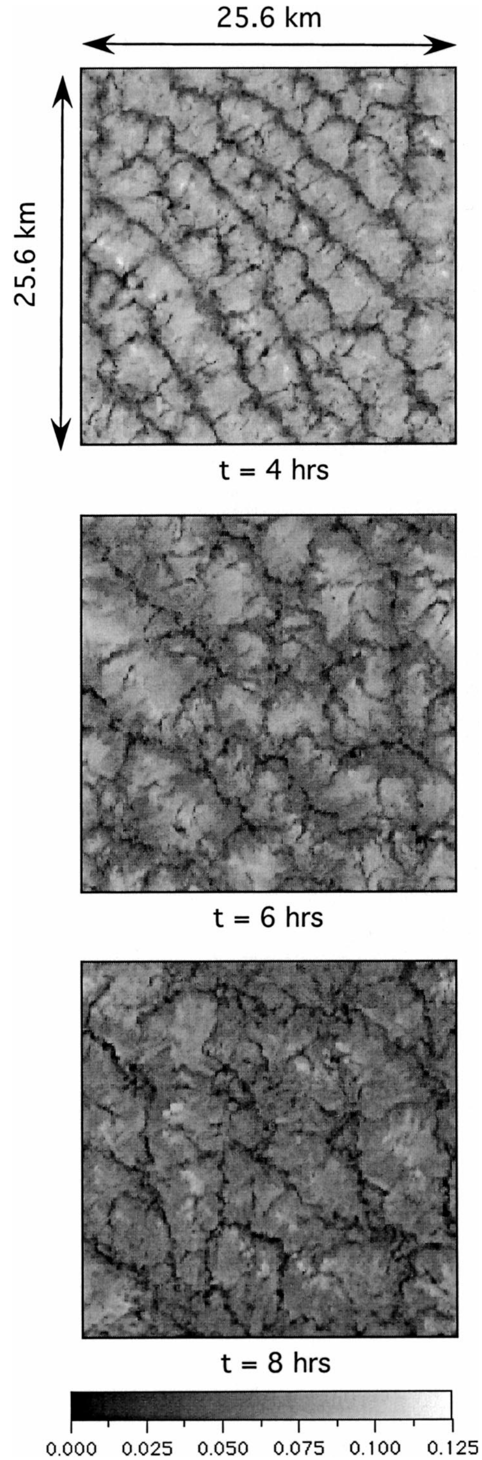

FIG. 10. The liquid water path of the stratocumulus simulation at t = 4, 6, and 8 h. The units of the numbers of the scale bar are kg m^{-2}.

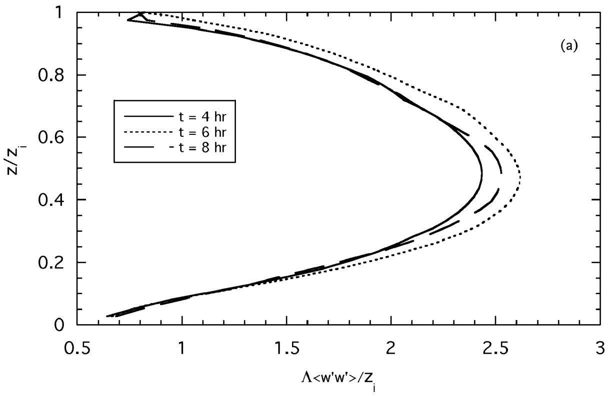

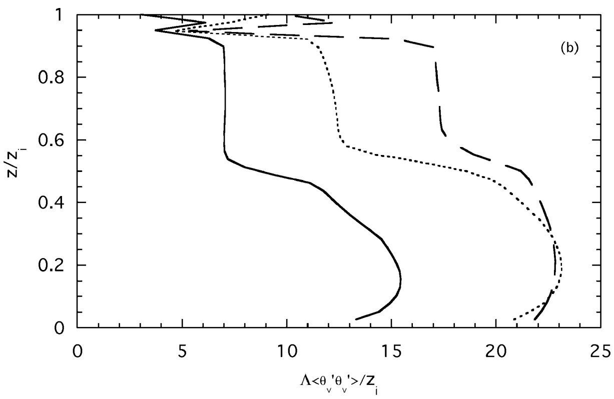

FIG. 11. Length scales normalized by the boundary layer depth (Λ/z_i) as a function of dimensionless height (z/z_i) for the STBL at t = 4, 6, and 8 h. Shown are the length scales for (a) the vertical velocity $\Lambda_{\langle w'w'\rangle}$ and (b) the virtual potential temperature $\Lambda_{\langle\theta_v'\theta_v'\rangle}$. Line styles are according to the legend displayed in the (a).

$$w_* = \left(2.5\frac{g}{\theta_0}\int_0^H \langle w'\theta_v'\rangle\, dz\right)^{1/3}, \tag{26}$$

with H the top of the boundary layer. Recall that the surface buoyancy flux for the radiatively cooled convective boundary layers is nearly the same as for the surface-driven CBL. In agreement with this notion are the findings by Fiedler and Khairoutdinov (1994), who concluded that for a boundary layer with a constant (positive) buoyancy flux mesoscale fluctuations in $\langle\theta_v'^2\rangle$ grow much more rapidly than for a CBL. As mentioned in the introduction, this paper follows a rather phenomenological approach. We do not focus on the cause but merely on the necessary ingredients for mesoscale generation, as well as on the consequences of it. In the next section we will briefly discuss a few observations which we consider relevant. In particular, the role of the buoyancy flux and the mean vertical stability will be discussed. Next we raise the issue of the lateral domain size.

4. Discussion

a. Variance production

The relevance of the buoyancy flux on the production of variance of the dynamic quantities is obvious since it is the primary production term in the variance equations for w and θ_v (Stull 1988),

$$\frac{\partial\langle w'w'\rangle}{\partial t} = 2\frac{g}{\theta_0}\langle w'\theta_v'\rangle - \frac{\partial\langle w'w'w'\rangle}{\partial z} - \frac{2}{\rho_0}\left\langle w'\frac{\partial p'}{\partial z}\right\rangle - 2\epsilon_w, \tag{27}$$

$$\frac{\partial\langle\theta_v'\theta_v'\rangle}{\partial t} = -2\langle w'\theta_v'\rangle\frac{\partial\langle\theta_v\rangle}{\partial z} - \frac{\partial\langle w'\theta_v'\theta_v'\rangle}{\partial z} - 2\epsilon_{\theta_v}, \tag{28}$$

where the third-order moments represent transport terms, ϵ_w and ϵ_{θ_v} represent net losses due to eddy viscosity, and the pressure term in (27) acts to redistribute vertical momentum into horizontal directions. In (28) we have neglected the effect of diabatic sources or sinks such as horizontally inhomogeneous radiation or latent heat release effects. After combining the production terms in (27) and (28), indicated by P_{w^2} and $P_{\theta_v^2}$, respectively, we find

$$P_{w^2} = 2\frac{g}{\theta_0}\langle w'\theta_v'\rangle = -\frac{g}{\theta_0}\left(\frac{\partial\langle\theta_v\rangle}{\partial z}\right)^{-1}P_{\theta_v^2}. \tag{29}$$

Note that for the spectral space an identical relation is applicable. Equation (29) indicates that only at levels where the boundary layer is unstably stratified a positive buoyancy flux acts to generate fluctuations of $\langle\theta_v'^2\rangle$ and $\langle w'^2\rangle$ simultaneously. Because entrainment of warm air from above the inversion stabilizes the upper part of the CBL, this implies that P_{w^2} and $P_{\theta_v^2}$ no longer work in concert. In particular, in the upper part of the CBL a negative buoyancy flux tends to dampen $\langle w'^2\rangle$, but due to the stable stratification $\langle\theta_v'^2\rangle$ is produced. The opposite occurs in the so-called countergradient flux regime, a layer in the middle of the CBL where the vertical flux and the vertical mean gradient of θ_v have the same sign (Holtslag and Moeng 1991).

To compute the production rate of variance P_{χ^2} for any arbitrary scalar, we can apply the linear superposition principle,

$$\begin{aligned}P_{\chi^2} &= -2\langle w'\chi'\rangle\frac{\partial\langle\chi\rangle}{\partial z}\\ &= -2a^2\left(\langle w'\psi'\rangle\frac{\partial\langle\psi\rangle}{\partial z} + r^2\langle w'\phi'\rangle\frac{\partial\langle\phi\rangle}{\partial z}\right.\\ &\qquad\left. + r\langle w'\psi'\rangle\frac{\partial\langle\phi\rangle}{\partial z} + r\langle w'\phi'\rangle\frac{\partial\langle\psi\rangle}{\partial z}\right),\end{aligned} \tag{30}$$

where we used Eqs. (13) and (14). It is found that the production term P_{χ^2} can obtain a negative value. In particular, $P_{\chi^2} < 0$, for negative flux ratios only. For -1

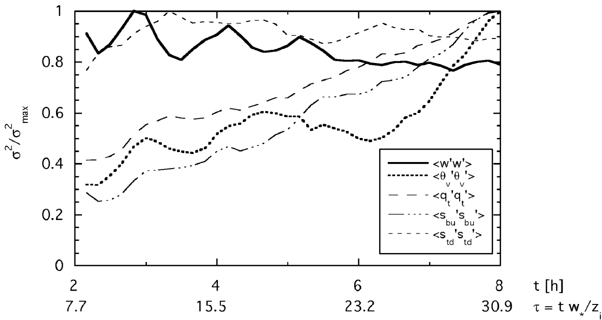

FIG. 12. Variance evolution in the middle of the STBL ($z/z_i = 0.5$) for the vertical velocity w, the virtual potential temperature θ_v, the total specific humidity q_t, and the bottom-up s_{bu} and top-down s_{td} scalars. The lower x-axis scale indicates the normalized, nondimensional time, $\tau = tw_*/z_i$. The variances are normalized by their respective maximum values. Line styles are according to the legend.

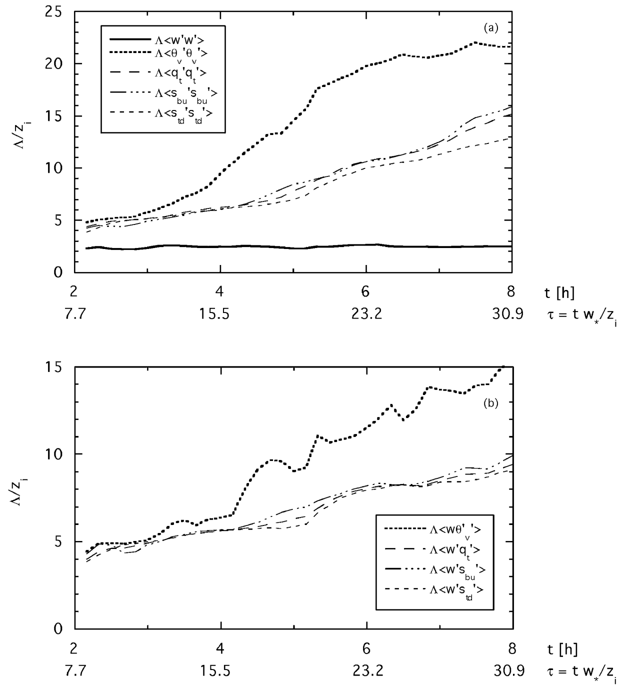

FIG. 13. Evolution of the length scale normalized by the boundary layer depth (Λ/z_i) in the middle of the STBL ($z/z_i = 0.5$). The lower x-axis scale indicates the normalized, nondimensional time, $\tau = tw_*/z_i$: (a) variance, (b) flux. Line styles are according to the legend.

$< r < 0$, the depth of the vertical layer where the production term is negative is most significant (de Roode et al. 2002). This finding is likely to be connected to the asymmetry in the length scales in the CBL around $r = 0$ shown in Fig. 7.

The change in the geometry of the buoyancy flux affects the variances for w and θ_v, of which the vertically integrated values after 8 hours of simulation are summarized in Table 2. It shows that both the vertical velocity variance as well as the virtual potential temperature variance are enhanced if the cooling rate at the top of the boundary layer is increased. Moreover, this corresponds to an increase in the length scales in the middle of the boundary layer for these two quantities (Fig. 15). Figure 16a corroborates the notion that enhanced virtual potential temperature fluxes in the interior of the boundary layer lead to an increase in the vertical velocity variance, as is the case for the smoke cloud simulations. The increase in vertically integrated θ_v variance for the smoke cloud cases appears to be mainly caused by a larger production rate of variance in the inversion layer, as is shown in Figure 16b.

Besides longwave radiative cooling, the stratocumulus case is also affected by wet-thermodynamics. If the total water content exhibits mesoscale fluctuations, this can directly lead to mesoscale fluctuations of the virtual potential temperature. As a reason, in saturated conditions θ_v fluctuations read (Nicholls 1984)

$$\theta_v' = \beta\theta_l' + \left(\beta\frac{L_v}{c_p} - \langle\theta_v\rangle\right)q_t', \tag{31}$$

with $\beta \sim 0.52$ a weak function of temperature, L_v the latent heat of vaporization, and c_p the specific heat of dry air at constant pressure. Multiplication of (31) by w' and slab averaging gives an identical expression for $\langle w'\theta_v'\rangle$. As is shown in Fig. 17 for the middle of the cloud layer, the total water flux gives the dominant contribution to the virtual potential temperature flux in the cloud layer. This implies that the contribution of θ_l' to θ_v' is negligibly small, and consequently $\theta_v' \approx [\beta(L_v/c_p) - \langle\theta_v\rangle]q_t'$. Because in the cloud layer we find that $P_{q_t^2} > 0$, the strong connection between q_t and θ_v fluctuations implies that both quantities have a positive variance production rate. This is a major difference with the interior of the CBL for which θ_v fluctuations are damped by a negative production rate, $P_{\theta_v^2} < 0$. The fact that w fluctuations do not become dominated by mesoscale fluctuations means that pressure fluctuations must be very efficiently redistributing vertical velocity fluctuations into horizontal directions. Nevertheless, the net effect is that in stratocumulus relatively more energy of the vertical velocity is present at mesoscales in comparison to the CBL. Since the production rate of variance is proportional to the magnitude of the vertical velocity fluctuations, one can appreciate why the mesoscale contribution to the (passive/active) scalar variance is much larger in the stratocumulus case. The second mechanism that supports the growth of θ_v perturbations is the longwave radiation field, which in the stratocumulus case depends on the local liquid water path and therefore causes a horizontally inhomogeneous cooling. Last, fluctuations in the horizontal wind field are produced by wind shear near the surface, which may affect the structure of the vertical velocity field.

b. The LES horizontal domain size: How large is large enough?

In all LES cases considered, the evolution of significant mesoscale fluctuations was observed. Even in the

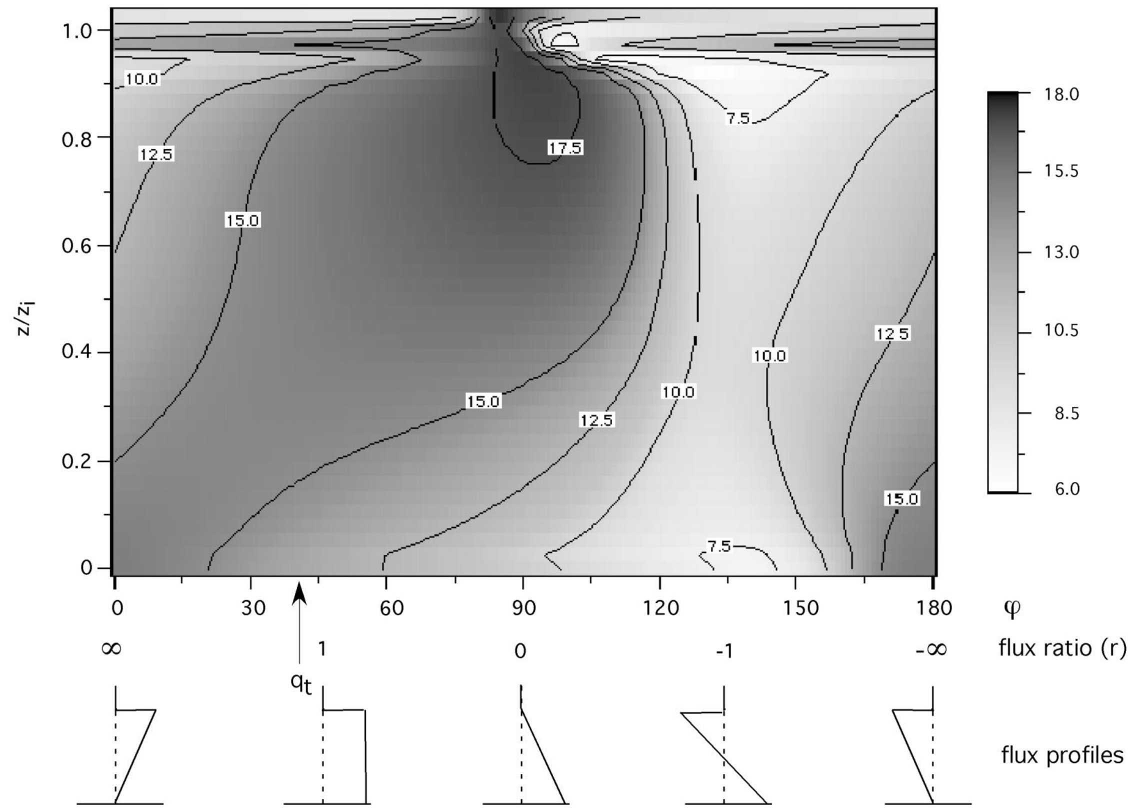

FIG. 14. Length scales normalized by the boundary layer depth (Λ/z_i) in the STBL at $t = 8$ h. The length scales are shown as a function of the dimensionless height (z/z_i) and the flux ratio angle φ according to Eq. (22). The lower x-axis label indicates a few corresponding flux ratios r, and the corresponding vertical flux profiles are displayed below. In addition, the flux ratio for the total specific humidity is indicated by the vertically pointing arrow.

CBL, where the buoyancy field does not exhibit significant broadening, dynamically active scalars such as moisture and potential temperature acquire dominating mesoscale fluctuations. In Figs. 6 and 13a one observes that the length scale growth is a rather slow yet steady process. This shows the importance of the lateral domain size: sooner or later the effect of the lateral boundaries will be felt as they constrain further increase of the horizontal length scales.

To show the role of the domain size on the development of the variance spectra three additional stratocumulus cases have been simulated on different domain sizes, namely, 3.2, 6.4, and 12.8 km. The horizontal grid resolution is taken the same as for the large domain simulation. Figure 18 displays the variance spectra of the vertical velocity and specific humidity. On the basis of the vertical velocity spectrum a domain size of 3.2 km seems sufficient since for wavenumbers smaller than 10^{-3} m^{-1} the contribution to the variance decreases rapidly, implying that the most energetic eddy sizes are well resolved in the simulation. In contrast, the total specific humidity variance spectrum points out that the location of the spectral peak coincides with the domain size, except for the simulation on the largest horizontal domain. Because in the spectral space the q_t fluctuations grow predominantly on the mesoscales, their contribution to the total variance will become increasingly important. Obviously, if the horizontal domain size is too small such that these mesoscale fluctuations cannot be represented, this will lead to an underestimation of the variance.

It is important to note that the mesoscale fluctuations also have a gradually increasing contribution to the vertical transport (fluxes), as revealed by Fig. 13b: one-third of the buoyancy flux is governed by scales larger than $15z_i$ (9 km), for example, and considering the evolution in time, this number will continue to increase. The same holds for the transport of moisture, potential temperature, and passive scalars (chemical species, pollutants, etc).

The strong impact of mesoscale fluctuations on the vertical transport touches upon an important issue at the core of the LES concept. Briefly, the philosophy of LES is that the transport is primarily carried out by the most ''energetic'' eddies. These eddies, which have a typical scale on the order of the PBL depth, are therefore fully resolved in the simulation, while eddies smaller than a predefined filter size are modeled. However, the essential point to be made here based on the results presented is that the ''mesoscale eddies'' are *hardly energetic* as

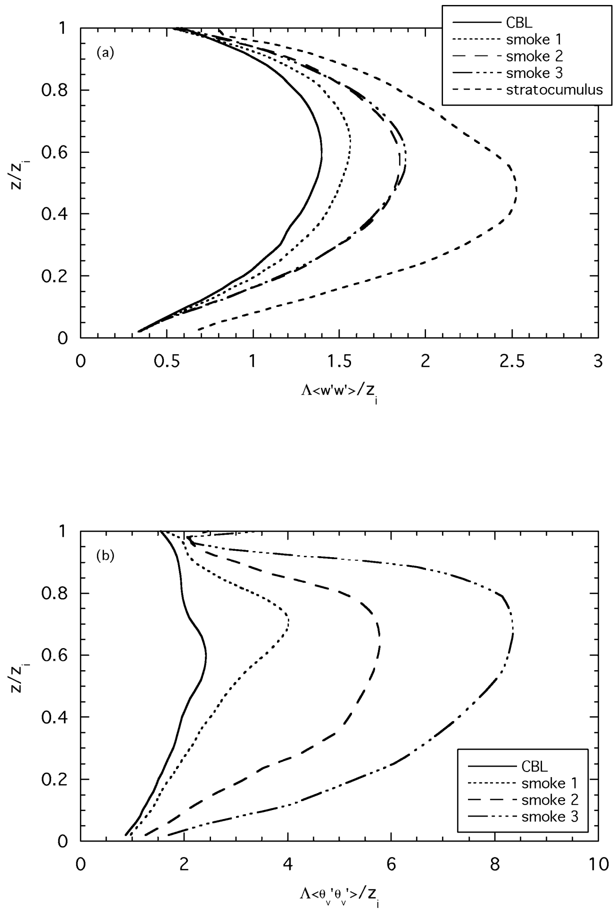

FIG. 15. Length scales normalized by the boundary layer depth (Λ/z_i) as a function of dimensionless height (z/z_i) for the radiatively cooled convective boundary layers (smoke 1–3) at $t = 8$ h. Shown are the length scales for (a) the vertical velocity $\Lambda_{\langle w'w'\rangle}$ and (b) the virtual potential temperature $\Lambda_{\langle \theta_v' \theta_v' \rangle}$. In addition, the length scales for w and θ_v in the CBL, and w in the STBL are shown to facilitate easy comparison. Line styles are according to the legend.

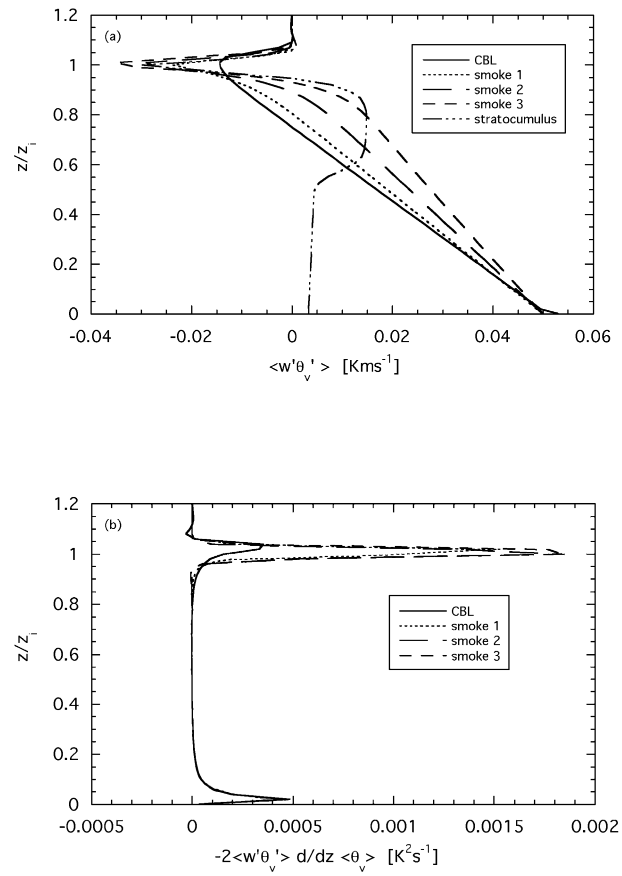

FIG. 16. Vertical mean profiles during the last hour of the simulation ($7 < t \leq 8$ h). (a) The virtual potential temperature flux. (b) The production term of $\langle \theta_v'^2 \rangle$ variance. Line styles are according to the legend.

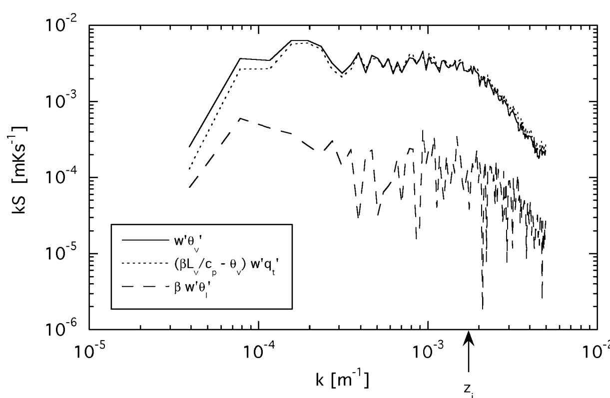

FIG. 17. Covariance spectra S in the middle of the stratocumulus cloud layer ($z/z_i = 0.75$) at $t = 8$ h for the vertical fluxes of the virtual potential temperature θ_v, and for the total specific humidity q_t and the liquid water potential temperature θ_l multiplied by factors, according to (31), to give their contribution to the virtual potential temperature flux. The wavenumber corresponding to the reciprocal of the boundary layer depth z_i is indicated by the vertically pointing arrow.

can be seen in the w variance spectra (e.g., Figs. 2 and 18a), yet they do have a big impact on the variance and transport of nearly all quantities (Figs. 6, 13, and 15). The cure is simple, though: the lateral domain size should be chosen large enough to resolve these large-scale fluctuations so as to allow for their (autonomous) development.

The answer to the question raised in the title depends, on the one hand, on the type of convection to be simulated and the kind of physical question one wishes to address, and, on the other hand, the total simulation time. If one aims to investigate the dynamics of a dry CBL, that is, one without moisture, a rather small horizontal domain size suffices since the dominant length scale of the buoyancy field is about $(1 \sim 2)z_i$ and hardly changes with time. However, if one incorporates moisture or passive scalars to study their turbulent transport, it seems necessary to increase the horizontal domain size. The evolution of large scales is slow, but steady;

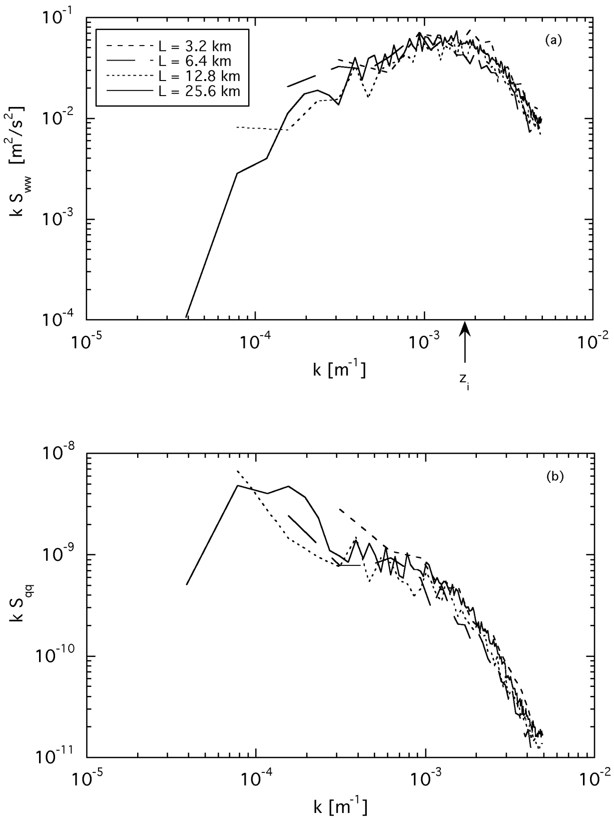

FIG. 18. Variance spectrum S multiplied by the wavenumber k just above the stratocumulus cloud base ($z/z_i = 0.6$) for four different domain sizes (L). (a) The vertical velocity w, and (b) the total specific humidity q_t. Line styles are according to the legend in the upper panel. The wavenumber corresponding to the reciprocal of the boundary layer depth z_i is indicated by the vertically pointing arrow.

larger scales take more time to develop. Phrased differently, if one has chosen a relatively long integration time, the domain size should be relatively large. Simulations of the CBL on longer time scales can be relevant for mixed layers that are advected over the oceans by the mean wind. Such conditions may favor the formation of shallow cumulus clouds, the typical scale of which will be determined by the distribution of heat and moisture in the subcloud layer (Jonker et al. 1999b). The evolution of length scales in the stratocumulus-topped boundary layer appears to be more dramatic. Whether the horizontal domain size is large enough is easily assessed by calculating the variance and covariance spectra and considering the contribution from the large scales (order domain size). One might be momentarily pleased with a spectral power law (say $k^{-5/3}$) extending all the way to the smallest wavenumber, but in our view such a result is indicative of an insufficiently large lateral domain.

For a boundary layer that is in a quasi-steady state, the vertical fluxes of conserved variables vary linearly with height, and are thus determined by the fluxes at the bottom and the top of the boundary layer. Since the vertical gradient of the vertical flux determines the tendency of the mean quantities, it is reassuring in this context that the horizontal domain size appears to have only a limited influence on the temporal evolution of mean quantities. For the CBL we find that the horizontal slab-mean value of the vertical flux of any arbitrary quantity is only marginally modified, although its precise spatial distribution may depend on the horizontal domain size. Although for different horizontal domain sizes there appears to be more variation in the results for the buoyancy flux and the vertical velocity variance in stratocumulus, quantities like the cloud-base and cloud-top height evolution seem not to be very sensitive.

5. Summary and conclusions

Several large-eddy simulations performed on a large horizontal domain (25.6×25.6 km^2) have been discussed.

A clear convective boundary layer in which the surface fluxes of moisture and potential temperature equally contribute to the surface buoyancy flux has been studied. It is found from the variance spectra of the virtual potential temperature and the vertical velocity that the most energetic eddies have scales with sizes on the order of the boundary layer depth. In contrast, for the same case both the specific humidity as well as the potential temperature field exhibit significant mesoscale fluctuations. At these scales specific humidity and potential temperature fluctuations are anticorrelated to a high degree.

Mesoscale fluctuations are also dominating the variance spectra of bottom-up and top-down scalars in the clear convective boundary layer. By means of a linear superposition of variables, the variance spectrum of any arbitrary conserved passive scalar could be reconstructed. The variance spectra of variables with different entrainment to surface flux ratios (r) were analyzed. It was shown that for flux ratios in the range near $r \approx -0.25$, the mesoscale fluctuations from the bottom-up and top-down fields nearly completely cancel each other. Therefore, only for flux ratios close to this number the variance spectra are dominated by fluctuations with scales of the order of the boundary layer depth, whereas for any other flux ratio mesoscale fluctuations become significant.

In stratocumulus, all scalars (active and passive) become dominated by mesoscales fluctuations, including the virtual potential temperature. Also, the length scale for the vertical velocity in the stratocumulus-topped boundary layer is larger than in the clear convective boundary layer.

Consideration of the production terms in the prognostic variance equations for the vertical velocity and the virtual potential temperature reveals the importance of the vertical stability of the CBL. For an unstable stratification, a positive virtual potential temperature flux acts to produce both vertical velocity as well as virtual potential temperature variance. In contrast, for a stable stratification production of either virtual potential temperature variance or vertical velocity variance is suppressed. Because there is a stable stratification in the middle of the CBL, the positive virtual potential temperature fluxes lead to a destruction of virtual potential temperature variance.

The geometry of the buoyancy flux was manipulated by cooling the clear convective boundary layer from the top in addition to a positive buoyancy flux at the surface. We found that the length scales of both vertical velocity as well as virtual potential temperature tend to increase if the (horizontally homogeneous) cooling rate is amplified. These simulations corroborate results from other studies that showed that latent heat effects due to condensation/evaporation are not a necessary ingredient responsible for the generation of cell broadening (Fiedler and Khairoutdinov 1994; Shao and Randall 1996; Müller and Chlond 1996; Dörnbrack 1997). Although various mechanisms were proposed in these papers, the cases studied have in common that broader cells seem to be related to changes in the *geometry* of the buoyancy flux. In particular, in this study it appears that cell broadening is caused by an increase in the convective velocity due to enhanced buoyancy fluxes in the interior of the boundary layer. For the radiatively cooled convective boundary layers the increase in the vertical velocity variance is likely to be attributed to this mechanism, whereas the production of virtual potential temperature variance is most notably increased near the inversion layer.

For the stratocumulus case, evaporation and condensation of cloud liquid water droplets affect the buoyancy flux. For the stratocumulus case studied it is found that the positive buoyancy flux in the middle of the cloud layer is dominated by the total specific humidity flux, and the contribution of the liquid water potential temperature flux to the buoyancy flux is negligibly small. Therefore, if the total specific humidity has fluctuations at mesoscales, this will directly enforce mesoscale fluctuations in the buoyancy.

The CBL results reveal that diabatic effects, such as radiation and latent heat release, are not essential for the generation of mesoscale fluctuations. This holds not only for passive scalars, but also for dynamically active scalars as potential temperature and specific humidity. Diabatic effects are important, though, for speeding up and enhancing the process. The magnitude of the vertical velocity fluctuations in the mesoscale range plays an important role in determining the growth rate of the variance for (passive/active) scalars at the mesoscales. We have shown that mesoscale fluctuations in the vertical velocity get enhanced if processes like radiative cooling or latent heat release effects are included, and this is found to coincide with an increasing importance of mesoscale fluctuations in the variance spectra of passive scalars.

The simulations of the clear and the radiatively cooled CBLs show that the autonomous development of mesoscale fluctuations is apparently inherent to buoyancy-driven convection. Although the magnitude of vertical fluxes does not depend very much on the horizontal domain size, mesoscale fluctuations affect the spectral distribution of the vertical transport, but more importantly, they can have a strong impact on the variance of various quantities. The location of the spectral peak of any arbitrary quantity at the end of the simulation can be regarded as a check whether the domain size is sufficiently large. If the spectral peak is located nearby, or even at the domain size, then the lateral domain size is unmistakably too small. In that case, the length scale will be erroneously constrained by the horizontal domain size of the model. We showed that a large domain size is not necessary if one aims to study the dynamics of a clear CBL, that is, one without moisture, since the dominant length scale of the buoyancy is about $(1 \sim 2)z_i$, and hardly changes with time. In contrast, if one includes moisture or passive scalars to study their turbulent transport, one needs to increase the horizontal domain size. In the stratocumulus-topped boundary layer length scales of passive scalars grow more rapidly than in the CBL. In addition, the length scale of the buoyancy is also found to increase with time. These findings suggest that to study turbulence in stratocumulus clouds with an LES model a much larger horizontal domain size is recommended.

A steady growth of length scales has various implications for modeling and observational studies. If there is no well-defined spectral gap present in the variance spectrum of an arbitrary quantity, the separation between the subgrid and resolved contributions to the variance or its vertical flux is not straightforward. For a numerical weather prediction model this problem can become relevant if it has a horizontal grid spacing on the order of $\sim$10 km. Also, the lack of a well-defined spectral gap complicates the analysis of turbulence observations in the atmosphere since data are usually filtered to separate the turbulence from the mesoscale perturbations. Another important finding is that the variance is often not in a steady state. Such second-order moments are sometimes needed for microphysical or radiative computations in large-scale models, and simple assumptions like a balance between the production and dissipation of variance may lead to erroneous estimations.

The findings presented here are entirely based on modeling results. In general, it is difficult to verify the simulated length scale evolutions against observations made in the atmosphere. For example, fluctuations on any scale of any quantity will be caused if the surface and entrainment fluxes are horizontally inhomogeneous. To tackle these kind of problems one may perform experiments with a convective mixed layer in a laboratory tank (Deardorff and Willis 1985). If one utilizes a saline convection tank, as discussed by Hibberd and Sawford (1994), colored dye can be used to mimic a bottom-up or top-down scalar. A first goal of such an experiment would be to demonstrate that fluctuations of the latter tend to grow on scales much larger than the boundary layer depth.

Acknowledgments. The investigations were supported by the Netherlands Organization for Scientific Research (NWO). This work was sponsored by the National Computing Facilities Foundation (NCF) for the use of supercomputer facilities. We like to thank Bjorn Stevens for many interesting discussions. The comments of David Lewellen, and two anonymous reviewers have helped to improve the manuscript.

APPENDIX

Flux Ratios of Temperature and Specific Humidity

For a boundary layer that is capped by an infinitesimally thin inversion layer, the turbulent flux at the top of the mixed layer is given by,

$$\langle w'\chi'\rangle_T = -w_e\Delta\langle\chi\rangle. \tag{A1}$$

By (15) the entrainment rate can then be expressed as

$$w_e = -r_{\theta_v}\frac{\langle w'\theta_v'\rangle_0}{\Delta\theta_v}. \tag{A2}$$

Typical values in the CBL are $r_{\theta_v} \approx -0.1, \ldots, -0.3$. Assuming that both the inversion jumps $\Delta\langle q\rangle$, $\Delta\langle\theta\rangle$ and the surface fluxes $\langle w'q'\rangle_0$, $\langle w'\theta'\rangle_0$ are given, one can derive the flux ratios r_θ and r_q with aid of (21), (A1), and (A2):

$$r_\theta = r_{\theta_v}\left(\frac{1 + \dfrac{0.61\langle\theta\rangle\langle w'q'\rangle_0}{\langle w'\theta'\rangle_0}}{1 + \dfrac{0.61\langle\theta\rangle\Delta\langle q\rangle}{\Delta\langle\theta\rangle}}\right) \quad \text{and} \tag{A3}$$

$$r_q = r_{\theta_v}\left(\frac{1 + \dfrac{\langle w'\theta'\rangle_0}{0.61\langle\theta\rangle\langle w'q'\rangle_0}}{1 + \dfrac{\Delta\langle\theta\rangle}{0.61\langle\theta\rangle\Delta\langle q\rangle}}\right). \tag{A4}$$

In clear convective boundary layers one typically observes $\Delta\langle q\rangle < 0$, $\Delta\langle\theta\rangle > 0$, $\langle w'q'\rangle_0 > 0$, and $\langle w'\theta'\rangle_0 > 0$. Since $\Delta\langle\theta_v\rangle$ must be positive, there is the additional constraint $\Delta\langle\theta\rangle > -0.61\langle\theta\rangle\Delta\langle q\rangle$. These conditions yield $r_q > 0$ and $r_\theta < r_{\theta_v}(<0)$.

REFERENCES

Agee, E. M., 1984: Observations from space and thermal convection: A historical perspective. *Bull. Amer. Meteor. Soc.,* **65,** 938–946.

Albrecht, B. A., D. A. Randall, and S. Nicholls, 1988: Observations of marine stratocumulus clouds during FIRE. *Bull. Amer. Meteor. Soc.,* **69,** 618–626.

Atkinson, B. W., and J. W. Zhang, 1996: Mesoscale shallow convection in the atmosphere. *Rev. Geophys.,* **34,** 403–431.

Bretherton, C. S., and Coauthors, 1999: An intercomparison of radiatively-driven entrainment and turbulence in a smoke cloud, as simulated by different numerical models. *Quart. J. Roy. Meteor. Soc.,* **125,** 391–423.

Cuijpers, J. W. M., 1994: Large-eddy simulation of cumulus convection. Ph.D. thesis, Technical University Delft, 150 pp.

Davis, A., A. Marshak, W. Wiscombe, and R. F. Cahalan, 1996: Scale invariance of liquid water distribution in marine stratocumulus. Part I: Spectral properties and stationary issues. *J. Atmos. Sci.,* **53,** 1538–1558.

Deardorff, J. W., 1973: Three-dimensional numerical modeling of the planetary boundary layer. *Workshop on Micrometeorology,* D. A. Haugen, Ed., Amer. Meteor. Soc., 271–311.

——, and G. E. Willis, 1985: Further results from a laboratory model of the convective planetary boundary layer. *Bound.-Layer Meteor.,* **32,** 205–236.

de Roode, S. R., P. G. Duynkerke, and H. J. J. Jonker, 2002: Countergradient fluxes in the clear convective boundary layer: The role of the entrainment flux. Preprints, *15th Symp. on Boundary Layers and Turbulence,* Wageningen, Netherlands, Amer. Meteor. Soc., 187–190.

Dörnbrack, A., 1997: Broadening of convective cells. *Quart. J. Roy. Meteor. Soc.,* **123,** 829–847.

Durand, P., F. Thoumieux, and D. Lambert, 2000: Turbulent lengthscales in the marine atmospheric mixed layer. *Quart. J. Roy. Meteor. Soc.,* **126,** 1889–1912.

Duynkerke, P. G., and S. R. de Roode, 2001: Surface energy balance and turbulence characteristics observed at the SHEBA ice camp during FIRE III. *J. Geophys. Res.,* **106,** 15 313–15 322.

——, and J. Teixeira, 2001: Comparison of the ECMWF reanalysis with FIRE I observations: Diurnal variation of marine stratocumulus. *J. Climate,* **14,** 1466–1478.

Fiedler, B. H., 1993: Cell broadening in three-dimensional thermal convection between poorly conducting boundaries. *Beitr. Phys. Atmos.,* **66,** 173–181.

——, and M. Khairoutdinov, 1994: Cell broadening in three-dimensional thermal convection between poorly conducting boundaries: Large eddy simulations. *Beitr. Phys. Atmos.,* **67,** 235–241.

Hibberd, M. F., and B. L. Sawford, 1994: A saline laboratory model of the planetary convective boundary-layer. *Bound.-Layer Meteor.,* **67,** 229–250.

Hignett, P., 1991: Observations of the diurnal variation in a cloud-capped marine boundary layer. *J. Atmos. Sci.,* **48,** 1474–1482.

Holtslag, A. A. M., and C. H. Moeng, 1991: Eddy diffusivity and countergradient transport in the convective atmospheric boundary layer. *J. Atmos. Sci.,* **48,** 1690–1698.

Jonker, H. J. J., P. G. Duynkerke, and J. W. M. Cuijpers, 1997: Energy spectra in the mesoscale range: An LES study. Preprints, *12th Symp. on Boundary Layers and Turbulence,* Vancouver, BC, Canada, Amer. Meteor. Soc., 225–226.

——, ——, and ——, 1999a: Mesoscale fluctuations in scalars generated by boundary layer convection. *J. Atmos. Sci.,* **56,** 801–808.

——, ——, and A. P. Siebesma, 1999b: Development of mesoscale fluctuations in cloud topped boundary layers. Preprints, *13th Symp. on Boundary Layers and Turbulence,* Dallas, TX, Amer. Meteor. Soc., 197–200.

Kaimal, J. C., J. C. Wyngaard, D. A. Haugen, O. R. Cote, Y. Izumi, S. J. Caughey, and C. J. Readings, 1976: Turbulence structure in the convective boundary layer. *J. Atmos. Sci.,* **33,** 2152–2169.

Khanna, S., and J. G. Brasseur, 1998: Three-dimensional buoyancy and shear-induced local structure of the atmospheric boundary layer. *J. Atmos. Sci.,* **55,** 710–743.

Krishnamurti, R., and L. N. Howard, 1981: Large-scale flow generation in turbulent convection. *Proc. Natl. Acad. Sci. USA,* **78,** 1981–1985.

Lenschow, D. H., and B. B. Stankov, 1986: Length scales in the convective boundary layer. *J. Atmos. Sci.,* **43,** 1198–1209.

——, J. Mann, and L. Kristensen, 1994: How long is long enough when measuring fluxes and other turbulence statistics? *J. Atmos. Oceanic Technol.,* **11,** 661–673.

Mahrt, L., E. Moore, and D. Vickers, 2001: Dependence of turbulent

and mesoscale velocity variances on scale and stability. *J. Appl. Meteor.,* **40,** 628–641.
Mason, P. J., 1989: Large-eddy simulation of the convective atmospheric boundary layer. *J. Atmos. Sci.,* **46,** 1492–1516.
Müller, G., and A. Chlond, 1996: Three-dimensional numerical study of cell broadening during cold-air outbreaks. *Bound.-Layer Meteor.,* **81,** 289–323.
Nicholls, S., 1978: Measurements of turbulence by an instrumented aircraft in a convective atmospheric boundary layer over the sea. *Quart. J. Roy. Meteor. Soc.,* **104,** 653–676.
——, 1984: The dynamics of stratocumulus: Aircraft observations and comparisons with a mixed layer model. *Quart. J. Roy. Meteor. Soc.,* **110,** 783–820.
——, 1989: The structure of radiatively driven convection in stratocumulus. *Quart. J. Roy. Meteor. Soc.,* **115,** 487–511.
——, and M. A. LeMone, 1980: The fair weather boundary layer in GATE: The relation of subcloud fluxes and structure to the distribution and enhancement of cumulus clouds. *J. Atmos. Sci.,* **37,** 2051–2067.
Nucciarone, J. J., and G. S. Young, 1991: Aircraft measurements of turbulence spectra in the marine stratocumulus-topped boundary layer. *J. Atmos. Sci.,* **48,** 2382–2392.
Oncley, S. P., C. A. Friehe, J. C. Larue, J. A. Businger, E. C. Itsweire, and S. S. Chang, 1996: Surface-layer fluxes, profiles, and turbulence measurements over uniform terrain under near-neutral conditions. *J. Atmos. Sci.,* **53,** 1029–1044.
Rothermel, J., and E. M. Agee, 1980: Aircraft investigation of mesoscale cellular convection during AMTEX 75. *J. Atmos. Sci.,* **37,** 1027–1049.
Rudnick, D. L., and R. Ferrari, 1999: Compensation of horizontal temperature and salinity gradients in the ocean mixed layer. *Science,* **283,** 526–529.
Schröter, M., and S. Raasch, 2002: Broadening of convective cells during cold air outbreaks: A high resolution study using a parallelized LES model. Preprints, *15th Symp. on Boundary Layers and Turbulence,* Wageningen, Netherlands, Amer. Meteor. Soc., 45–48.
Shao, Q., and D. A. Randall, 1996: Closed mesoscale cellular convection driven by cloud-top radiative cooling. *J. Atmos. Sci.,* **53,** 2144–2165.
Siebesma, A. P., and J. W. M. Cuijpers, 1995: Evaluation of parametric assumptions for shallow cumulus convection. *J. Atmos. Sci.,* **52,** 650–666.
Stull, R. B., 1988: *An Introduction to Boundary Layer Meteorology.* Kluwer Academic, 666 pp.
Sykes, R. I., W. S. Lewellen, and D. S. Henn, 1988: A numerical study of the development of cloud-street spacing. *J. Atmos. Sci.,* **45,** 2556–2569.
VanDelden, A., 1992: The dynamics of meso-scale atmospheric circulations. *Phys. Rep.,* **211,** 251–374.
Van der Hoven, I., 1957: Power spectrum of horizontal wind speed in the frequency range from 0.0007 to 900 cycles per hour. *J. Meteor.,* **14,** 160–164.
VanZanten, M. C., 2000: Entrainment processes in stratocumulus. Ph.D. thesis, Utrecht University, 139 pp.
Wyngaard, J. C., and R. A. Brost, 1984: Top-down and bottom-up diffusion of a scalar in the convective boundary layer. *J. Atmos. Sci.,* **41,** 102–112.
Young, G. S., 1987: Mixed layer spectra from aircraft measurements. *J. Atmos. Sci.,* **44,** 1251–1256.